A Predictive Model of Separations in Dead-End Filtration with Ultrathin Membranes

Karl J. P. Smith[1], Marina May[1], Ruth Baltus[2], James L. McGrath[1*]

[1] *University of Rochester, Rochester, NY*

[2] *Clarkson University, Potsdam, NY*

Abstract

Nanoporous Silicon Nitride (NPN) is a new ultrathin (50 nm thick) membrane with potential applications in laboratory and industrial preparations of nanoparticles, antibodies, and other therapeutic biotechnology products. Like prior ultrathin silicon-based membranes (nanomembranes), NPN is capable of high separation resolution (∼10 nm) despite polydisperse pore distributions. Here we present a mathematical model that is predictive of the sieving curves seen in dead-end filtration with NPN. Interestingly, the model requires the inclusion of concentration polarization to predict sieving curves. The model also reveals a pressure dependence on sieving curves that is highly sensitive to membrane thickness: Thicker membranes require higher, often impractical, pressures for the same separations while thinner membranes achieve sharp separations at lower pressures. The pressure sensitivity of sieving behavior is confirmed experimentally by comparing the performance of NPN with 10 μm thick nanoporous polycarbonate track etched membranes. The model illustrates that pore polydispersity limits the resolution of current silicon nanomembranes, suggesting that further manufacturing advancements are needed to realize the full potential of nanomembranes for size-based separations. Finally, the model further suggests that diffusion across ultrathin membranes aids separations, leading to

*Corresponding author

Email address: jmcgrath@bme.rochester.edu (James L. McGrath[1])

URL: nanomembranes.org (James L. McGrath[1])

higher resolution even in iso-flux conditions.

Keywords: Nanoporous, ultrafiltration, sieving, concentration polarization
2010 MSC: 00-01, 99-00

1. Introduction

Nanoporous membranes are critical to research and industrial processes such as biotech preparations, human hemodialysis, and scientific preparations of biologicals and nanoparticles. A standard therapeutic biotech product utilizes between 10-20 membrane-based steps [1], while 250 million hemodialysis membranes were sold in the US alone in 2013 [2]. The membranes used for these processes are typically polymeric and sponge-like, with high internal surface areas and broad effective pore distributions [3]. New nanomembranes typically have hydraulic permeabilities that are many orders of magnitude higher than polymeric membranes [4, 5], and can distinguish between similarly sized particles during filtration [6]. These benefits suggest a growing role for ultrathin and hyperthin membranes as regulatory standards regarding the purity of biological compounds become increasingly rigorous and the industry moves past highly active compounds such as hormones to products like monoclonal antibodies that require much higher dosages for therapeutic effect [3].

The first practical nanomembranes were porous nanocrystalline silicon (pnc-Si). First reported in 2007 [7], pnc-Si membranes are manufactured using standard lithography, heating, and etching processes. Pnc-Si membranes are 15-30 nm thick, have relatively narrow pore size distributions that are tunable within the range of 5-35 nm in diameter, and have hydraulic permeabilities 1000x that of thicker commercial membranes. While pnc-Si membranes fulfill many of the requirements for next generation ultrafiltration membranes, they are both chemically unstable [8] and mechanically unreliable. New nanoporous nitride (NPN) membranes, which are made using pnc-Si membranes as a pore template, were developed to overcome the limitations of pnc-Si [9]. These membranes are about twice as strong as pnc-Si and are more chemically stable because of the inert

nature of silicon nitride but retain the high permeability and size selectivity of pnc-Si [9].

While the hydraulic and diffusive permeability of ultrathin membranes can be explained from existing theories [4, 10, 11], there have been no theories to explain their sieving function. Like pnc-Si, NPN is remarkably good at size discrimination of nanoparticles [9, 12], and so we hypothesized that thinness promotes excellent size selectivity. Here we test this hypothesis by developing a predictive analytic model and comparing experimental results from NPN to thick track etched (TE) membranes with similar pore sizes. Our results confirm that thinness promotes size discrimination but reveal unexpected mechanisms. First, we find that the phenomena of concentration polarization promotes sharper separations in dilute solute conditions. Because the high permeability of nanomembranes promotes concentration polarization, they display sharp sieving curves at low pressures. Additionally, we find that nanomembranes are thin enough that diffusive transport contributes significantly to transmembrane flux, whereas convection dominates solute transport across thick membranes.

2. Theoretical Model

To develop a predictive model of the separation behavior of ultrathin membranes, we begin with the sieving coefficient S, which for a gold nanoparticle separation is defined as the ratio of final concentration of gold in the filtrate C_{filtrate} to the concentration of the stock solution C_{stock}

$$S = \frac{C_{\text{filtrate}}}{C_{\text{stock}}} \tag{1}$$

C_{filtrate} is a time-dependent quantity in dead-end filtration, and can be defined as:

$$C_{\text{filtrate}}(t) = \frac{\int_0^t Q_{\text{gold}} dt}{\int_0^t Q_{\text{water}} dt} \tag{2}$$

where Q_{gold} and Q_{water} are the gold and water fluxes through the membrane, with units of moles/$m^2 s$ and $m^3/m^2 s$, respectively.

Because the hydraulic resistance is governed by the hydrodynamics of the nanopores, the solvent flux through a single pore can be by extending the Hagen-poiseille equation to include short pores [10]:

$$Q_{\text{water}} = \frac{\Delta P r^3}{\mu\left[3 + \frac{8}{\pi}\left(\frac{l}{r}\right)\right]} A \tag{3}$$

where A, μ, r, and l are the open area of the membrane, solvent viscosity, pore radius, and pore length, respectively. For this model, we assume that the hydraulic resistance of the membrane is unchanged over the course of the experiment so that

$$\int_0^t Q_{\text{water}} dt = \frac{\Delta P r^3}{\mu\left[3 + \frac{8}{\pi}\left(\frac{l}{r}\right)\right]} At = V(t) \tag{4}$$

With $V(t)$ representing the volume of water that has passed through the membrane at time t.

The instantaneous gold flux thorough the membrane is the sum of the diffusive and convective fluxes through the membrane. The diffusive solute flux is given by Fick's Law of Diffusion as $Q_{\text{gold, diffusion}} = -D_\infty \frac{dC}{dy}$, where D_∞ is the diffusivity of a solute molecule as given by the Stokes-Einstein equation and dC is the concentration gradient through the pore. Because of steric and electrostatic interactions, the free diffusion of particles is 'hindered' by the walls of the pore, so that the diffusive term is actually $Q_{\text{gold, diffusion}} = -K^{-1} D_\infty \frac{dC}{dy}$, with a diffusive hindrance factor (also called the enhanced drag) K^{-1} [13]. Similarly, purely convective transport can characterized by $Q_{\text{gold, convection}} = GvC$, with v representing the bulk flow rate and G the convective hindrance factor (also called the lag coefficient) [13]. Adding these contributions gives

$$Q_{\text{gold}} = Q_{\text{gold, diffusion}} + Q_{\text{gold, convection}} = -K^{-1} D_\infty \frac{dC}{dy} + GvC \tag{5}$$

[14]

Deen derived the following system of equations to describe solute flux Q_{gold} in terms of these parameters and a particle/pore interaction energy:

$$Pe = \frac{W\langle v\rangle l}{H D_\infty} \tag{6}$$

$$H = 2\int_0^{1-\alpha} K^{-1} e^{-E(\beta)/kT} \beta d\beta \tag{7}$$

$$W = 4\int_0^{1-\alpha} G(1-\beta^2) e^{-E(\beta)/kT} \beta d\beta \tag{8}$$

$$\langle Q_{\text{gold}} \rangle = W \langle v \rangle C_{\text{stock}} \frac{[1 - (C_{\text{after}}/C_{\text{before}})e^{-Pe}]}{1 - e^{-Pe}} \tag{9}$$

[14] where $\beta = \frac{\text{radial position}}{r}$ is the dimensionless radial position, Pe is the Péclet number (the ratio of convective to diffusive transport in the system), $\alpha = \frac{\text{particle radius}}{\text{pore radius}}$, and $E(\beta)$ is the potential energy describing the interaction between a particle and the pore wall. H and W are two hydrodynamic functions that modify the diffusive and convective flux (respectively) due to steric and electrostatic contributions to the energy of interaction. Brackets ($\langle\rangle$) indicate a radial average and K^{-1} and G are interpolated from Paine and Scherr's numerical simulations[13]. Our formulation of $E(\beta)$ is from Smith and Deen's model of solute partitioning within a charged pore[15] (details in S.I. Section 1). Surface charge densities for NPN membranes are derived from experimentally measured zetapotentials (details in S.I. Section 3).

C_{after} and C_{before} in Equation 9 refers to the ratio of the concentration of gold downstream of the membrane to the gold upstream of the membrane. Stokes drag pulls the particles away from the membrane on the downstream side. For this reason, the downstream side is assumed to be well mixed, so that $C_{\text{after}} = C_{\text{filtrate}}$. However, on the upstream side, Stokes drag pulls the particles towards the membrane. When transport toward the membrane occurs faster than particles enter the membrane, there is a buildup of particles and we cannot assume $C_{\text{before}} = C_{\text{stock}}$. Instead we must calculate the actual concentration at the membrane surface C_{membrane}. With these changes Equation 9 becomes:

$$\langle Q_{\text{gold}} \rangle = W \langle v \rangle C_{\text{stock}} \frac{[1 - (C_{\text{filtrate}}/C_{\text{membrane}})e^{-Pe}]}{1 - e^{-Pe}} \tag{10}$$

If we consider the gold that does not make it through the membrane (in units

of moles):

$$n_{\text{rejected}}(t) = V(t)C_{\text{stock}} - n_{\text{filtrate}}(t) \tag{11}$$

Where V is the volume of water that has passed through the membrane, and n_{filtrate} is the moles of gold in the filtrate, which is given by

$$n_{\text{filtrate}}(t) = \int_0^t Q_{\text{gold}}(t)A dt \tag{12}$$

We can then relate these quantities back to S:

$$S = \frac{n_{\text{filtrate}}(t)}{V(t)} / C_{\text{stock}} \tag{13}$$

As rejected gold accumulates at the membrane surface it leads to a local concentration jump, so that $C_{\text{membrane}} >> C_{\text{stock}}$. This also means that $C_{\text{membrane}}(t)$ is time dependent. If we assume the distribution of rejected gold particles is governed by a quasi-equilibrium balance between the viscous drag of solvent pulling them towards the membrane and diffusion away from the membrane surface, as pictured in Figure 1, the distribution can be described by Poisson-Boltzmann statistics.

$$C_{\text{rejected}}(h,t) = C_{\text{rejected}}(0,t)e^{\frac{-6\pi\mu Rvh}{kT}} \tag{14}$$

where C(h,t) is the concentration of gold at a height h above the surface of the membrane at time t, $C_{\text{rejected}}(0,t)$ is the concentration of rejected gold at the surface of the membrane, $6\pi\mu Rv$ is the Stokes drag on a single particle, and kT is the thermal energy. Note that this is the concentration of only the rejected gold, and the total gold concentration is found by superimposing the uniform stock concentration.

Before describing the case of partial rejection of gold nanoparticles by the membrane it is useful to consider the case of complete rejection ($S = 0$). Under these conditions we can integrate both sides of equation 14 with respect to height above the membrane:

$$\int_{h=0}^{h=\infty} AC_{\text{rejected}}(h,t)\mathrm{d}h = \int_{h=0}^{h=\infty} AC_{\text{rejected}}(0,t)e^{\frac{-6\pi\mu Rvh}{kT}}\mathrm{d}h \tag{15}$$

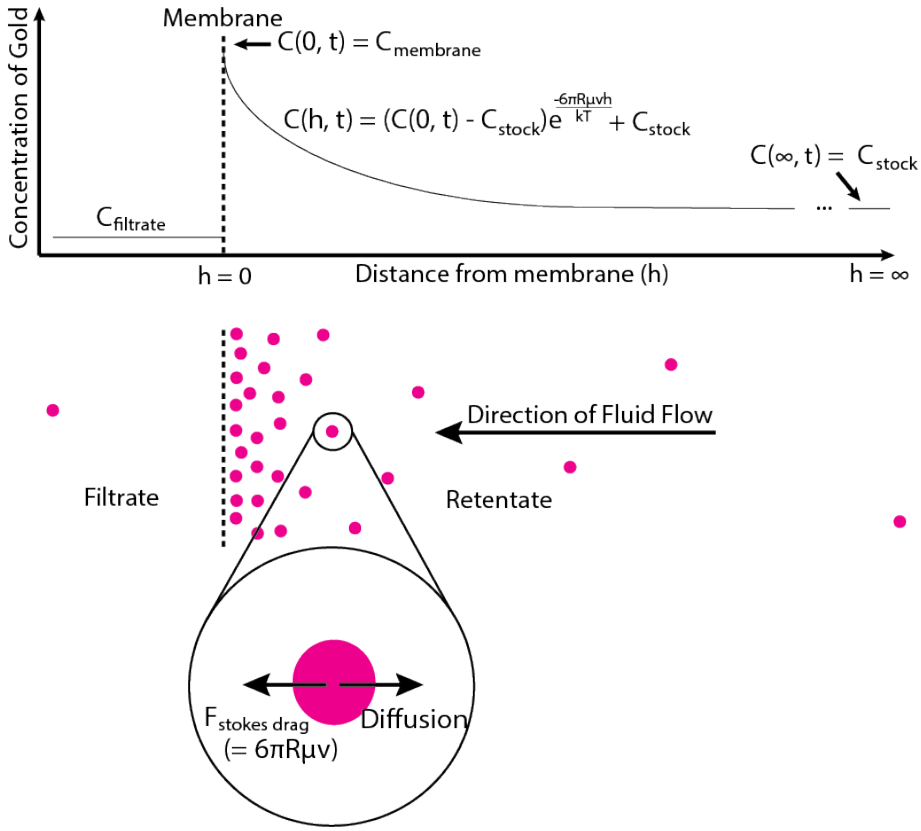

Figure 1: **Schematic of Particle Distribution for Particles Rejected by Membranes** The distribution is a quasi-equilibrium between convection towards the membrane and back diffusion, which is described by Poisson-Boltzmann statistics.

Note that the scale height of the Boltzmann distribution for a typical separation is given as:

$$\frac{kT}{6\pi R\mu v} \tag{16}$$

and will be on the order of 90 nm ($R = 40$ nm, $v = 6.4 \times 10^{-5} m/s$, while the typical fluid head height of a separation is 1.4 cm, which means $h_{max} = h_\infty$ is a reasonable approximation. The rejected population is equal to the filtrate volume times the stock concentration. This quantity can be thought of as the population that would have passed through the membrane if the membrane were completely permissive. With a perfectly rejecting membrane, this population must instead end up behind the membrane in the Boltzmann distributed rejected fraction:

$$V(t)C_{\text{stock}} = -\frac{kT}{6\pi R\mu v} A C_{\text{rejected}}(0,t) * (e^{-\frac{6\pi R\mu v(\infty)}{kT}} - e^{-\frac{6\pi R\mu v(0)}{kT}}) \tag{17}$$

Where

$$C_{\text{rejected}}(0,t) = \frac{V(t)C_{\text{stock}}}{A}\frac{6\pi R\mu v}{kT} \tag{18}$$

Substituting this result into Equation 14 gives a complete equation for the rejected gold at any height:

$$C_{\text{rejected}}(h,t) = \frac{V(t)C_{\text{stock}}}{A}\frac{6\pi R\mu v}{kT} * e^{-\frac{6\pi R\mu v h}{kT}} \tag{19}$$

In the more general case that some gold passes through the membrane ($S \neq 0$) the rejected population will be reduced according to the mass balance in Equation 11. This changes Equation 19 to:

$$C_{\text{rejected}}(h,t) = \frac{(V(t)C_{\text{stock}} - n_{\text{filtrate}}(t))}{A}\frac{6\pi R\mu v}{kT} * e^{-\frac{6\pi R\mu v h}{kT}} \tag{20}$$

The concentration of rejected gold at the surface is correspondingly

$$C_{\text{rejected}}(0,t) = \frac{(V(t)C_{\text{stock}} - n_{\text{filtrate}}(t))}{A}\frac{6\pi R\mu v}{kT} \tag{21}$$

To get the final concentration at the membrane surface we add back the stock gold concentration:

$$C_{\text{membrane}}(t) = \frac{(V(t)C_{\text{stock}} - n_{\text{filtrate}}(t))}{A}\frac{6\pi R\mu v}{kT} + C_{stock} \tag{22}$$

Where C_{membrane} is the total concentration of gold at the mouth of the pore. Note that we assume the gold concentration is never high enough to form a cake or packed layer. The concentration at the membrane surface is substantially higher than the bulk concentration, with the model predicting a 2,100x increase in concentration at the membrane surface after passing 100 μL of 30 nm diameter gold through a membrane with 40 nm diameter pores, but even with this concentration increase, the initial gold is so dilute (the stock solution of 30 nm diameter gold has 2×10^{11} particles/mL [16]) that the average inter-particle spacing at the membrane is still 170 nm. This means that even in the low salt conditions of the separation (Debye length = 4.3 nm) particle-particle interactions can be ignored.

Equations 5-10 and 22 constitute a complete set of governing expressions that allow us to predict sieving coefficients for a given volume of filtrate and pore size. We solved the resultant differential equation through numerical integration in MATLAB (Mathworks.com), with 30 iterations over the passage of 100 μL of fluid through a standard NPN membrane showing excellent convergence. To account for pore distributions, the sieving coefficient is first calculated for each individual pore. Each of these coefficients is then weighed by the relative flux through its respective pore to get a total sieving coefficient.

$$S = \sum_{i=1}^{\gamma} S_i \frac{Q_i}{Q_{\text{total}}} \tag{23}$$

where γ is the number of pores in the membrane, and S_i is the sieving coefficient calculated for a single pore (13).

3. Experimental Methods

Two different NPN wafers [7, 9] with average pore minor axes of 55.7 $\pm$11.1 nm (wafer #2226) and 40.9 $\pm$7.8 nm (wafer #1146), and porosities of 24.4% and 17.1%, respectively, were provided by SiMPore Inc. (West Henrietta, NY). Pore size distributions and membrane porosity were determined using TEM images (Hitachi 7650) of the membranes and custom image processing software

that fits each pore to an ellipse (software available for download at nanomembranes.org/resources/software). Average pore sizes and porosity were compared at the center and the edge of each wafer and were found to vary no more than 1 nm and 2%, respectively. An Atomic Layer Deposition (ALD) system (Cambridge Nanotech) was used to lay down either 91 or 136 cycles of alumina (with a per-cycle thickness of ∼1.1 Angstrom) on chips from wafer #2226, to make chips with average pore minor axes of 21.2 ±7.9 nm and 13.7 ±6.9 nm and porosities of 5.8% and 1.8%, respectively. NPN membranes were assembled into custom plastic 'SepCon' housings with silicone gaskets cut from 1 μm thick sheets with a craft cutter (Silhouette Cameo) [9]. Sepcon vials were pre-loaded with 10 μL of Invitrogen UltraPure distilled water on both the front and back side of the membrane, since otherwise surface tension effects at the exit of the nanopores will prevent fluid flow [12].

Polycarbonate Track Etched (TE) membranes 13 mm in diameter with specified pore sizes of 50 nm (PCT00813100) and 80 nm (PCT00513100) were purchased from Sterlitech. TE membranes were affixed to the same Sepcon plastic housing, but using polydimethylsiloxane (PDMS) mixed from a kit (10:1, Sylgard 184 silicone elastomer kit) instead of pre-cut-and-cured silicone gaskets. Because of differences in surface chemistry, the back sides of TE membranes do not need to be pre-wet, but the front sides were still loaded with 10 μL of UltraPure water. Gold nanoparticles were purchased from BBI international in sizes of 5, 10, 15, 20, 30, 40, 50, 60, and 80 nm diameter. The actual size of each gold nanoparticle stock solution differed from the manufacturer values, and the real distributions were characterized using a TEM (S.I. Table 1).

During separations, 300 μL of a gold nanoparticle solution was loaded above the membrane and the system was pressurized using a nitrogen tank. Pressure was monitored with a manometer (VWR, #8215), and the separation continued until ∼100 μL of fluid had passed unless otherwise noted. Filtrate gold concentrations were measured by comparing the absorbance at the peak (which varied between gold particle sizes over the range of 515 to 550 nm) to standard curves using a Tecan Infinite M200 plate reader and a quartz cuvette

(ZEN2112). The zetapotential of NPN and alumina-coated NPN was measured using a custom streaming potential rig (S.I. Section 3) while the zetapotential of the gold nanoparticles and TE membranes were supplied by the manufacturers [17, 16]. Salt concentration of the gold solutions was estimated based on the conductivity of the gold nanoparticle solutions (measured using an Oakton CON 6 Acorn series conductivity meter) from which the gold nanoparticles had been precipitated out by freezing.

4. Results

We first demonstrated that the model is predictive of size cutoffs and sieving coefficients over a wide range of pore-size-to-particle-size ratios. In these studies, atomic layer deposition (ALD) was used to create four distinct populations of chips with pore size distributions shown in Figure 2. Chips from wafer #2226 were subject to either 91 or 136 ALD cycles. Since ALD lays down alumina in successive monolayers, with each monolayer having an approximate thickness of ∼1.1 Angstrom, these cycle numbers were chosen to target an average pore diameter reduction of 20 and 30 nm, respectively. The addition of the alumina had the effect of making the pores slightly more oblong, likely due to interfacial effects. Note that ALD coats the membrane surface, not just the inside of the pores, so that the membranes with alumina are also slightly thicker. Each pore is fitted to an ellipse, and the minor axes of these ellipses are compared, since the minor axis is the limiting factor for spheres attempting to enter a pore.

In Figure 3, constant pressure (1.3 PSI) sieving experiments were done with a size ladder of gold nanoparticle solutions. Chips from each of the populations shown in Figure 2 were assembled into custom plastic housings and loaded with the gold nanoparticle size ladder. The resultant sieving curves, as well as model predictions for the same sieving curves are shown in Figure 3a. In Figure 3b, three different model curves are shown for just one pore size distribution, demonstrating that the best results come from a model that incorporates both concentration polarization and the polydispersity of the pore size distribution.

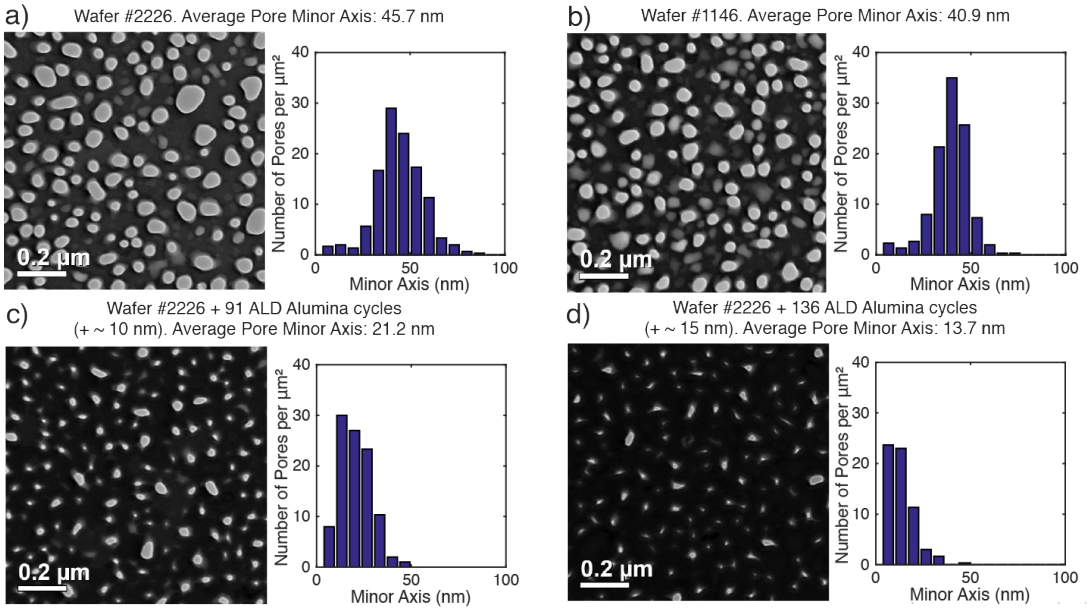

Figure 2: **Modification of Pore Size Distributions through Atomic Layer Deposition** We used two different NPN wafers (a and b) and two different ALD runs (c and d) to create a spectrum of four different pore size distributions. Note that adding alumina to the membrane shifts its pore size distribution leftward, and also narrows it, due to the hard bound at zero.

The model includes no fitting parameters, yet is still able to capture the location and shape of the sieving curves. The fact that the sieving coefficient plateaus below 1.0 suggests that ∼8% of the gold is lost during the separations - likely due to adsorption by the plastic housing. We chose not to include a correction for this to preserve the lack of free parameters in our model.

Given that concentration polarization is essential for proper predictions by our model, we reasoned that any factors affecting the particle distribution near the membrane should affect sieving curves. The first way we sought to shift the particle distribution was by varying the flux of particles to the membrane. We reasoned that an increased flux implies an enhanced Stokes drag towards the membrane, therefore a decrease in scale height (Equation 16), and enhancing transport near the cut-off. Simulations shown in Figure 4a support these expectations for membranes with the thickness of graphene, NPN, and TE mem-

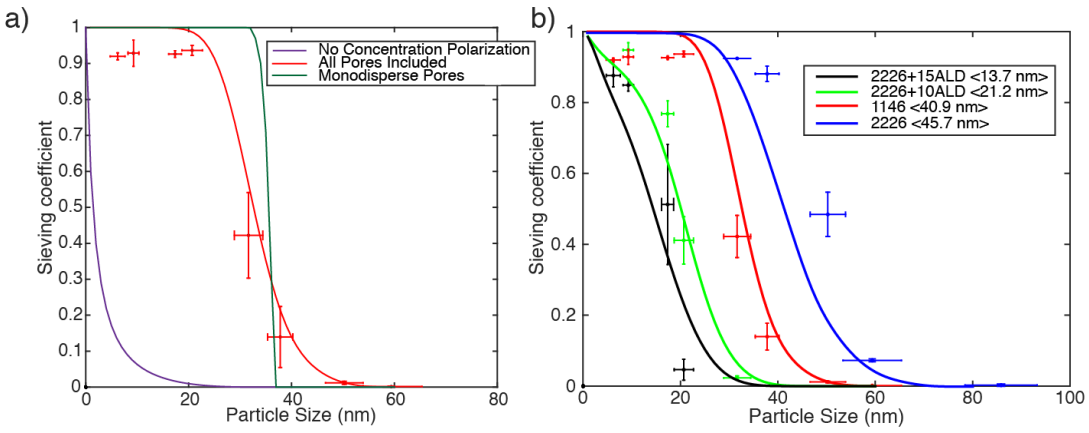

Figure 3: **Gold Sieving Model Predictions and Experimental Data** a) Using the four membrane populations from Figure 2, we found that our model is predictive of the sharp transitions characteristic of gold nanoparticle separations with NPN membranes across a variety of particle size to pore size ratios. b) A sieving model that fails to account for concentration polarization behind the membrane does a poor job of predicting experimental sieving behavior of gold nanoparticles through an NPN membrane, while modeling NPN as a collection of perfectly uniform pores results in a sieving cutoff sharper than that experimentally seen. A model that includes both concentration polarization and the real pore size distribution fits the data the best of the three models.

branes. Each membrane thickness shows a sharper sieving curve as pressure is increased between 1.3 and 10 PSI. The influence of pressure on sieving curves are pronounced for thick TE membranes, modest for NPN membranes, and subtle for theoretical graphene membranes. Clearly higher flows are expected with thinner membranes for a given pressure, thus the effect of reducing membrane thickness is again to decrease the scale height of the particle distribution and improve transport near the cut-off.

To experimentally test the trends of Figure 4a we sought TE membranes with the same number of pores (5×10^7) and size of pores ($\sim$50 nm) as our standard NPN chips. With these conditions, a difference in convective flux between the two membranes under similar pressures should be only due to differences in the membrane thickness. Commercially available TE membranes with manufacturer specified pores of 50 nm were available at $\sim$1% porosity for a total of 4×10^7pores (see Methods). While the active membrane area of NPN chips was much lower (1.5×10^{-6} m^2) than the area of TE membranes (2.5×10^{-5} m^2), the porosity of NPN is much higher (24%) and thus the number of pores active during a filtration experiment would be comparable between the two membranes (NPN: $\sim 6 \times 10^7$; TE: $\sim 4 \times 10^7$). Sieving curves with these TE membranes indeed show a sensitivity to pressure between 1.3 and 10 PSI while experiments, with NPN showed a very modest, but statistically detectable, change shift in sieving with increased pressure (Figure 4b). While these trends match the predictions of our simulations, the matched TE membranes exhibited cut-offs near 20 nm instead of the expected 50 nm. We verified the manufacturer's claims of 50 nm pore sizes at the membrane surface by electron microscopy (not shown). We suspect that the etch processes that creates such small pore membranes is thick materials not effective in the bulk of the 10 μm membrane so that the pores narrow in the middle to create smaller effective pore sizes. Since these smaller than expected pores diameters will increase membrane resistance significantly, we also examined the pressure sensitivity of TE membranes with commercially specified pores of 80 nm (Figure 4b). The sieving curves of these membranes behaved as expected and again showed a significant pressure sensitivity. With

larger pore diameters as NPN but in similar total number, these experiments with 80 nm TE membranes clearly point to membrane thickness as the reason for pressure sensitivity in sieving curves.

Another way to increase the degree of concentration polarization is simply to filter longer. Consistent with this we show in supplemental data (SI Figure 3) that the filtration of 200 μL rather than our standard processes of 100 μL also shifts sieving curves very slightly to the right. The fact that the effect of longer filtration times is so small gives us confidence in that the analysis with 100 μL of filtrate is a reliable indicator of sieving curves. Our model accurately predicts this shift with larger filtration times (S.I. Figure 3).

The predictive quality of our mathematical model gives us the confidence to further study the mechanisms of ultrathin membrane performance in silico. We begin by defining the resolution implied by a sieving curve as:

$$\text{resolution} = \frac{\Delta x}{\bar{x}} \tag{24}$$

where Δx = (diameter of gold where $S = 0.1$) − (diameter of gold where $S = 0.9$) and $\bar{x}$ is the average of the two diameters used in Δx. The resolution is thus a measure of the difference between two particle sizes that a membrane can clearly separate in a dead-end filtration process. As shown in Figure 5a, our model predicts an improvement in resolution as membranes get thinner at a given pressure. It is also noteworthy that the sensitivity of the resolution to thickness is strongest at the size of TE and ultrafiltration membranes (1 μm - 10 μm), while resolution becomes relatively insensitive to thickness below ∼100 nm, particularly at higher pressures (>1.3PSI). This result highlights the emerging theme of our study: nanomembranes achieve separation performance at lower pressures that thicker materials can only achieve at much higher pressures

If improved resolution was simply due to convection-related phenomena, we should expect that matching the solvent flow rate with different membrane thicknesses to produce identical sieving curves. We will refer to these matched conditions as 'isoflux'. We found isoflux conditions by setting the driving pressures for simulated TE membranes and adjusting the driving pressure in simulations

for membranes with NPN (60 nm) and graphene (1 nm) thicknesses. All simulated membranes had the same number of pores ($\sim 6 \times 10^7$) and size of pores (50 nm) as our standard NPN chips. Results shown in Figure 5b indicate that thinner membranes still exhibit sharper sieving curves under isoflux conditions, suggesting that diffusion is acting as a second mode of transport across the thin membranes. We confirmed this by calculating the Peclet number (Pe = ratio of convective to diffusive transport; Eq. 6) for each simulated point in Figure 5b (Figure 5c, solid lines). The results show that diffusion actually dominates (Pe $<<1$) transport for NPN and graphene under these conditions while convection is the primary mode of transport across TE membranes for all but the smallest particles. Because these simulations are done for a low flow situation (i.e. matched to convective flow through a TE membrane with 50 nm pores and 1% porosity at 1.3 PSI), we repeated the simulations with flux matched instead to 10 PSI through TE membranes (Figure 5c, dashed lines). Under these conditions, transport across NPN membranes approaches a balance between convection and diffusion modes for larger particles while transport across theoretical graphene remains diffusion dominated at all particles sizes. Because the pressures simulated for NPN membranes were still lower than typically used in the laboratory, we then calculated Pe for a range of more practical pressures (Figure 5d). The results here show that nanomembranes operate in an interestin regime where transport may switch between diffusion dominated or convection dominated depending on only a small increase in applied pressure.

5. Discussion

With applications ranging from hemodialysis [18, 19] to molecular sensing [20], ultrathin nanoporous silicon membranes (nanomembranes) are poised to make significant contributions to science and technology in the coming decade. Adoption of these materials will occur if their increased costs compared to polymer membranes are outweighed by their value in solving separation problems. Efforts to improve manufacturing by making stronger materials with greater

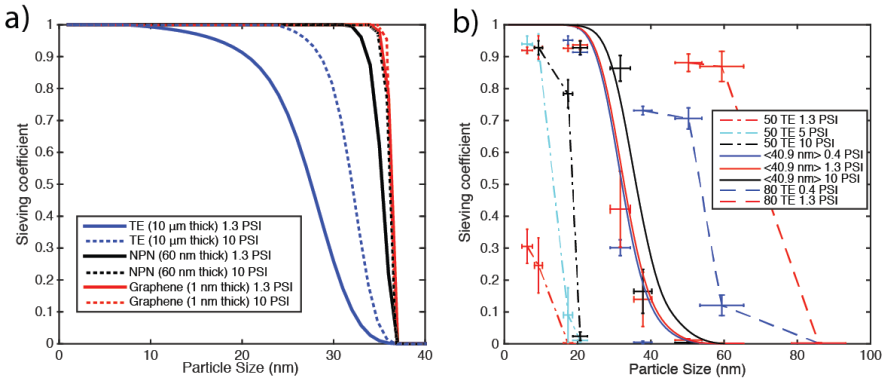

Figure 4: **The Effect of Membrane Thickness and Pressure on Sieving Curves** a) The sieving curves at two different pressures are shown for three different membranes membranes with uniform pores of 40.9 nm and thickness of 10 μm, 60 nm, and 1 nm, corresponding roughly to the thicknesses of TE, NPN, and 2-D graphene or graphene oxide membranes. b) A direct comparison between the sieving behavior of NPN and two different sizes of TE membranes at various pressures. Solid lines represent model calculations using the real distribution of pores. We find that the sieving curves of NPN membranes are weakly (but still significantly) dependent on pressure, and our model is predictive of this.

yield [9] and to increase active area [21, 19] focus on one half of this value proposition. Equally important are efforts to demonstrate and understand the character of separations with nanomembranes.

While the high permeability of nanomembranes follows directly from their thinness and can be explained with simple fluid models [12, 9], an understanding of their ability to distinguish between similarly sized particles has remained elusive. In this work we developed the first predictive model of the sieving behavior of nanomembranes. We have learned that the key feature explaining high resolution separations is the concentration of small rejected particles near the membrane surface (concentration polarization). Because the rejected particles are small enough to fit through the membrane in a second pass attempt, the rejection is temporary, but the concentration build-up helps drive transport across the membrane near the cut-off. For ultrathin membranes this build-up occurs at very modest pressures ($\sim$1 PSI; $\sim$6.8 KPa) leading to sharp sieving curves in

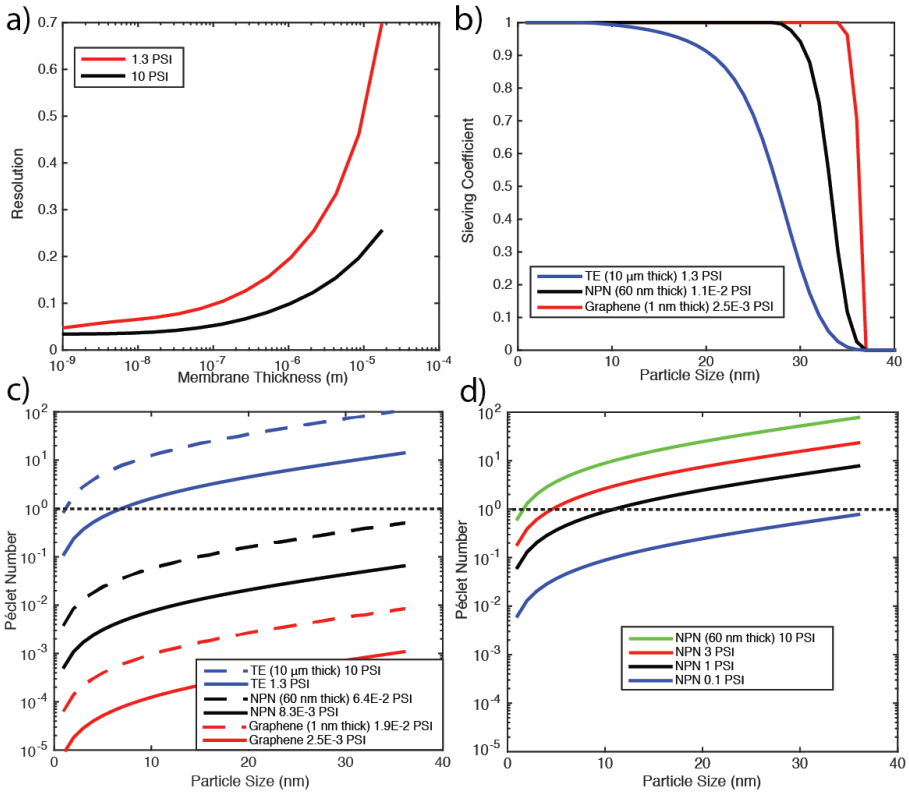

Figure 5: **Mechanistic Studies with Predictive Model** a) The benefit of thinner membranes is quantified by plotting membrane thickness *vs.* resolution at two different pressures based on model predictions. b) Model predictions of the sieving behavior of uniform pore distributions at various thicknesses, operated under different pressures to achieve the same flux through the membranes. c) Péclet number for the separations performed in b (solid line) as well as separations with the same membranes at a higher isoflux condition. Note that once the Péclet number of TE rises above one (i.e. the separation is dominated by convection) its performance begins deviating from that of NPN. d) Comparison of the Péclet number for NPN at different pressures. A two order of magnitude change in applied pressure can change a separation from dominated by diffusion at all gold sizes smaller than the pores to one dominated by convection for all gold sizes.

practical settings. While the same sharp sieving curves can occur with thicker materials, the lower permeability will require significantly higher pressures. Indeed, to achieve the flux through an NPN membrane pressurized to 1.3 PSI, a TE membrane would need to be pressurized to 155 PSI. Similarly, the largest pore (∼35 nm pore; 300kDa cut-off Omega brand) polyethersulfone membrane from Pall is recommended to run at 14,000g in a centrifuge (∼340 PSI) using a similar device to ours over a similar time frame (minutes). Thus the real enhancement from ultrathin membranes is their ability to realize high resolution separations at low pressures. This should have many important benefits such as cost-saving in industrial settings by the elimination of high pressure pumps, the preservation of biological samples that denature at high pressures, and the elimination of clogging from the compression of sample against membrane surfaces, etc. Low pressure filtration is also essential to microfluidic applications where pressures are already high due to small channel dimensions. The inclusion of a highly resistive filter in a microfluidic device can further increase pressures to result in leaks and component damage.

Another interesting finding from our work is that nanomembranes operate in a regime where diffusive and convective contributions to transport across the membrane are nearly balanced, while for conventional membranes with micrometer scale thickness, diffusion is negligible. Atomically thin graphene or graphene oxide membranes have yet to be produced with the millions of pores needed to make a practical filter [22, 23], but if these were to someday be used in dead-end filtration they would operate exclusively in a diffusion transport regime despite the presence of high convective flows. Like convective flux, the diffusive flux of particles also benefits from the rapid concentration polarization seen with ultrathin membranes.

Not surprisingly, our results also highlight that the polydispersity of current silicon nanomembranes limits their resolution in separations (Figure 3a). Polydispersity has been a feature of silicon nanomembranes since the original materials were made from the self-assembly of pores in pure silicon (pnc-Si) [7, 24], although pore distributions in pnc-Si are known to be much tighter than

the log-normal distributions of standard ultrafiltration membranes [25]. Because NPN uses pnc-Si as a pore template, additional processing causes further broadening of the pore distribution [9]. While considerably more costly to fabricate to scale than NPN, track-etched nanoporous nitride membranes [26] are monodisperse at low porosity (1%) where pore merger during etching can be avoided avoided. With resolutions ∼10 nm [12, 9] and outstanding hydraulic permeability (300 mL/(min-bar-cm^2), the performance of nanomembranes is sufficiently improved compared to conventional materials that they should be considered as replacements for many processes requiring size-based separations. Monodisperse nanomembranes however, remain a manufacturing goal as these may allow size based separation of species as subtly different as monomeric vs. dimeric proteins in low pressure and rapid processes.

Finally we note that our work here was confined to dilute, rigid and uniform gold nanoparticles as a model solute. While we have shown high resolution separations are possible with proteins [12], the current conclusions about mechanism and performance still need to be verified for these more concentrated and flexible solutes. In our studies on fouling mechanisms for NPN, for example, we have seen subtle differences between gold, which is very dilute and does not appear to clog or form a cake in constant flux experiments, and polystyrene beads [27] and protein solutions [28], where after a period of separation the hydraulic permeability declines according to the classic cake fouling mechanism. The mathematical model developed here provides a foundation for future work on proteins or other biological molecules. With the fluidics and sieving reliably predicted for dilute rigid solutes, we can now focus on modeling the the complex dynamics of biomolecules flowing through the short pores of NPN.

References

[1] A. S. Rathore, A. Shirke, Recent developments in membrane-based separations in biotechnology processes: review, Prep Biochem Biotechnol 41 (4) (2011) 398–421. doi:10.1080/10826068.2011.613976.

[2] F. SE, C. KGaA, Annual report 2013, Tech. rep., Fresenius Medical Care AG and Co KGaA, Else-Kröner-Straße 1, Bad Homburg v. d. H. (2013).

[3] R. van Reis, A. Zydney, Bioprocess membrane technology, Journal of Membrane Science 297 (1-2) (2007) 16–50. doi:{10.1016/j.memsci.2007.02.045}.

[4] H. D. Tong, H. V. Jansen, V. J. Gadgil, C. G. Bostan, E. Berenschot, C. J. M. van Rijn, M. Elwenspoek, Silicon nitride nanosieve membrane, Nano Letters 4 (2) (2004) 283–287. doi:10.1021/nl0350175.
URL http://dx.doi.org/10.1021/nl0350175

[5] Silicon Nanomembranes: Fundamental Science and Applications, Wiley VHC, 2016.

[6] N. Ileri, P. Stroeve, A. Palazoglu, R. Faller, S. H. Zaidi, H. T. Nguyen, J. A. Britten, S. E. Letant, J. W. Tringe, Fabrication of functional silicon-based nanoporous membranes, Journal of Micro-Nanolithography MEMS and MOEMS 11 (1). doi:{10.1117/1.JMM.11.1.013012}.

[7] C. C. Striemer, T. R. Gaborski, J. L. McGrath, P. M. Fauchet, Charge-and size-based separation of macromolecules using ultrathin silicon membranes, Nature 445 (7129) (2007) 749–753.

[8] A. A. Agrawal, B. J. Nehilla, K. V. Reisig, T. R. Gaborski, D. Z. Fang, C. C. Striemer, P. M. Fauchet, J. L. McGrath, Porous nanocrystalline silicon membranes as highly permeable and molecularly thin substrates for cell culture., Biomaterials 31 (20) (2010) 5408–5417. doi:10.1016/j.biomaterials.2010.03.041.

[9] J. P. S. DesOrmeaux, J. D. Winans, S. E. Wayson, T. R. Gaborski, T. S. Khire, C. C. Striemer, J. L. McGrath, Nanoporous silicon nitride membranes fabricated from porous nanocrystalline silicon templates, Nanoscale 6 (18) (2014) 10798–10805. doi:Doi10.1039/C4nr03070b.

URL <GotoISI>://WOS:000341020700050http://pubs.rsc.org/en/content/articlepdf/2014/nr/c4nr03070b

[10] Z. Dagan, S. Weinbaum, R. Pfeffer, An infinite-series solution for the creeping motion through an orifice of finite length, Journal of Fluid Mechanics 115 (1982) 505–523. doi:10.1017/S0022112082000883.

[11] J. Snyder, A. C. Jr., D. Fang, T. Gaborski, C. Striemer, P. Fauchet, J. McGrath, An experimental and theoretical analysis of molecular separations by diffusion through ultrathin nanoporous membranes, Journal of Membrane Science 369 (1–2) (2011) 119 – 129. doi:http://dx.doi.org/10.1016/j.memsci.2010.11.056.
URL http://www.sciencedirect.com/science/article/pii/S0376738810009257

[12] T. R. Gaborski, J. L. Snyder, C. C. Striemer, D. Z. Fang, M. Hoffman, P. M. Fauchet, J. L. McGrath, High-performance separation of nanoparticles with ultrathin porous nanocrystalline silicon membranes, ACS Nano 4 (11) (2010) 6973–6981. arXiv:http://pubs.acs.org/doi/pdf/10.1021/nn102064c, doi:10.1021/nn102064c.
URL http://pubs.acs.org/doi/abs/10.1021/nn102064c

[13] P. Paine, P. Scherr, Drag coefficients for the movement of rigid spheres through liquid-filled cylindrical pores, Biophysical Journal 15 (10) (1975) 1087 – 1091. doi:http://dx.doi.org/10.1016/S0006-3495(75)85884-X.
URL http://www.sciencedirect.com/science/article/pii/S000634957585884X

[14] W. M. Deen, Hindered transport of large molecules in liquid-filled pores, AIChE Journal 33 (9) (1987) 1409–1425. doi:10.1002/aic.690330902.
URL http://dx.doi.org/10.1002/aic.690330902

[15] F. G. S. III, W. M. Deen, Electrostatic effects on the partitioning of spherical colloids between dilute bulk solution and cylindrical pores,

Journal of Colloid and Interface Science 91 (2) (1983) 571 – 590. doi:http://dx.doi.org/10.1016/0021-9797(83)90371-5.
URL http://www.sciencedirect.com/science/article/pii/0021979783903715

[16] BBI Solutions, Gold Nanoparticle Data.

[17] S. Corporation, Pcte product and performance characteristics (2015).
URL http://www.sterlitech.com/pcte-product-and-performance-characteristics.html

[18] T. Burgin, D. Johnson, H. Chung, A. Clark, J. McGrath, Analytical and finite element modeling of nanomembranes for miniaturized, continuous hemodialysis, Membranes 6 (1) (2016) 6. doi:10.3390/membranes6010006.
URL http://www.ncbi.nlm.nih.gov/pmc/articles/PMC4812412/

[19] D. G. Johnson, T. S. Khire, Y. L. Lyubarskaya, K. J. P. Smith, J.-P. S. DesOrmeaux, J. G. Taylor, T. R. Gaborski, A. A. Shestopalov, C. C. Striemer, J. L. McGrath, Ultrathin silicon membranes for wearable dialysis, Advances in Chronic Kidney Disease 20 (6) 508–515. doi:10.1053/j.ackd.2013.08.001.
URL http://dx.doi.org/10.1053/j.ackd.2013.08.001

[20] M. N. Kavalenka, C. C. Striemer, J.-P. S. DesOrmeaux, J. L. McGrath, P. M. Fauchet, Chemical capacitive sensing using ultrathin flexible nanoporous electrodes, Sensors and Actuators B: Chemical 162 (1) (2012) 22 – 26. doi:http://dx.doi.org/10.1016/j.snb.2011.11.076.
URL http://www.sciencedirect.com/science/article/pii/S0925400511010811

[21] J. J. Miller, R. N. Carter, K. B. McNabb, J.-P. S. DesOrmeaux, C. C. Striemer, J. D. Winans, T. R. Gaborski, Lift-off of large-scale ultrathin nanomembranes, Journal of Micromechanics and Microengineering 25 (1)

(2015) 015011.
URL http://stacks.iop.org/0960-1317/25/i=1/a=015011

[22] P. Zhang, L. Ma, F. Fan, Z. Zeng, C. Peng, P. E. Loya, Z. Liu, Y. Gong, J. Zhang, X. Zhang, P. M. Ajayan, T. Zhu, J. Lou, Fracture toughness of graphene, Nature Communications 5 (2014) 3782 EP –.
URL http://dx.doi.org/10.1038/ncomms4782

[23] A. K. Geim, Graphene: Status and prospects, Science 324 (5934) (2009) 1530–1534. arXiv:http://science.sciencemag.org/content/324/5934/1530.full.pdf, doi:10.1126/science.1158877.
URL http://science.sciencemag.org/content/324/5934/1530

[24] D. Z. Fang, C. C. Striemer, T. R. Gaborski, J. L. McGrath, P. M. Fauchet, Methods for controlling the pore properties of ultra-thin nanocrystalline silicon membranes, Journal of Physics: Condensed Matter 22 (45) (2010) 454134.
URL http://stacks.iop.org/0953-8984/22/i=45/a=454134

[25] S. Mochizuki, A. L. Zydney, Theoretical analysis of pore size distribution effects on membrane transport, Journal of Membrane Science 82 (3) (1993) 211 – 227. doi:http://dx.doi.org/10.1016/0376-7388(93)85186-Z.
URL http://www.sciencedirect.com/science/article/pii/0376738893851862

[26] W. Zhang, J. Li, L. Cao, Y. Wang, W. Guo, K. Liu, J. Xue, Fabrication of nanoporous silicon dioxide/silicon nitride membranes using etched ion track technique, Nuclear Instruments and Methods in Physics Research Section B: Beam Interactions with Materials and Atoms 266 (12–13) (2008) 3166 – 3169, ¡ce:title¿Radiation Effects in Insulators¡/ce:title¿ ¡ce:subtitle¿Proceedings of the Fourteenth International Conference on Radiation Effects in Insulators¡/ce:subtitle¿ ¡xocs:full-name¿Fourteenth International Conference on Radiation Effects in Insulators¡/xocs:full-name¿. doi:http://dx.doi.org/10.1016/j.nimb.2008.03.213.

URL http://www.sciencedirect.com/science/article/pii/S0168583X08004680

[27] J. D. Winans, K. J. P. Smith, T. R. Gaborski, J. A. Roussie, J. L. McGrath, Membrane capacity and fouling mechanisms for ultrathin nanomembranes in dead-end filtration, Journal of Membrane Science 499 (2016) 282–289. doi:http://dx.doi.org/10.1016/j.memsci.2015.10.053.
URL http://www.sciencedirect.com/science/article/pii/S0376738815302830

[28] K. J. P. Smith, J. Winans, J. McGrath, Ultrathin membrane fouling mechanism transitions in dead-end filtration of protein (50343) (2016) V001T15A001–.
URL http://dx.doi.org/10.1115/ICNMM2016-7989